Analog and digital control of graphene field effect transistor sensors with the Raspberry Pi

Jesus Gomez

A thesis

submitted in partial fulfillment of the

requirements for the degree of

Master of Science

University of Washington

2021

Committee:

John Devin MacKenzie

Bruce Hinds

Program Authorized to Offer Degree:

Materials Science and Engineering

University of Washington

Abstract

Analog and digital control of graphene field effect transistor sensors with the Raspberry Pi

Jesus Gomez

Chair of the Supervisory Committee:
John Devin MacKenzie
Department of Materials Science and Engineering

Graphene based sensing platforms have been used in the development of novel sensors requiring high sensitivity and discriminatory selectivity with much success in many recent research publications. This report discusses the integration, and theory of operation behind such devices, mainly commercially available platforms of graphene field effect transistors (GFET). These devices are easily controlled on a breadboard with Python run on the Raspberry Pi 4 with an Analog-to-Digital Controller (ADC) and Digital-to-Analog Controller (DAC) shield. The control circuit for GFET signal reading uses passive bypass and decoupling circuits to power a current-driven full-bridge resistance measurement across the GFET channel. Voltage values are read directly, stored, converted to resistance measures, and plotted with a Python automation script. The data collected clearly shows the channel resistance across the GFET actively controlled for signaling with a common gate architecture. The increase in channel resistance with increasing

voltage bias across the gate is indicative of several phenomena: formation of p-channel depletion layer buildup, parasitic capacitance arresting electron flow, trap quantum state activations across the graphene surface, band bending of the graphene Dirac zero-points in the presence of an electric potential field, as well as shunting electron tunneling in the $[000\bar{1}]$ direction into the Si (111) wafer substrate.

Analog and digital control of graphene field effect transistor sensors with the Raspberry Pi

By: Jesus Gomez
Materials Science and Engineering
University of Washington

Supervisors: Dr. J. Devin MacKenzie, Dr. Bruce J. Hinds

Abstract – Graphene based sensing platforms have been used in the development of novel sensors requiring high sensitivity and discriminatory selectivity with much success in many recent research publications. This report discusses the integration, and theory of operation behind such devices, mainly commercially available platforms of graphene field effect transistors (GFET). These devices are easily controlled on a breadboard with Python run on the Raspberry Pi 4 with an Analog-to-Digital Controller (ADC) and Digital-to-Analog Controller (DAC) shield. The control circuit for GFET signal reading uses passive bypass and decoupling circuits to power a current-driven full-bridge resistance measurement across the GFET channel. Voltage values are read directly, stored, converted to resistance measures, and plotted with a Python automation script. The data collected clearly shows the channel resistance across the GFET actively controlled for signaling with a common gate architecture. The increase in channel resistance with increasing voltage bias across the gate is indicative of several phenomena: formation of p-channel depletion layer buildup, parasitic capacitance arresting electron flow, trap quantum state activations across the graphene surface, band bending of the graphene Dirac zero-points in the presence of an electric potential field, as well as shunting electron tunneling in the $[000\bar{1}]$ direction into the Si (111) wafer substrate.

1. Introduction

Graphene is currently at the center of much contemporary research and development for electronics and sensing devices [1]–[9]. This is due to its interesting properties such as tunable bandgaps, biocompatibility, controllable photoexcitation, and photoemission to name a few properties of contemporary interest. Commercial GFET platforms built in NEMS foundries are gaining popularity for their relatively low cost of implementation; by saving the user the time and money that would otherwise be spent building and optimizing their own masking and fabrication process in-house. Commercial GFETs also have the benefit of a consistent channel response across multiple chips, necessary for reliable calibration in mass produced devices. These devices often have readily accessible graphene surfaces for tuning chemical or optical absorbance characteristic responses in the sensor platform. Thus, GFETs for biomarker detection on an electrically conductive and biocompatible surface are quickly growing in popularity as well.

Chemical biosensor platforms, tunable nanoscale lasers for optoelectronic devices, record-high heat sinks, cords that are lighter and many orders of magnitude stronger than steel, and many more possibilities are promised by researchers and futurists lauding graphene. Concerningly, perhaps to the point of placing it on a pedestal as a panacea to all our shortcomings in chemistry, physics, electronics, society, *et cetera*.

This work is an attempt to dissect away all the superfluous claims made and introduces the reader first to the scientific understanding of graphene. It focuses on the quantum electronic properties of graphene and its application to consumer electronics. The high electronic carrier mobilities in graphene and other graphitic materials like carbon nanotubes and quantum dots are of particular interest to electronics and electrothermal design applications. The high carrier mobility that gives graphene its high conductivity comes from ballistic electron transport across the delocalized π-orbitals in graphene, which will be explained in further detail later.

How delocalized orbitals are related to the mirrored and reflected symmetrical energy band eigenstates will be discussed as well.

Controlling the available states of graphene at the quantum scale is necessary to tune bandgaps and electronics. Unfortunately, controlling and measuring these states in graphene currently takes access to multibillion dollar facilities with tunneling microscopes and powerful, focused beam sources. Therefore, the financial cost of implementation for the most exotic graphene devices will remain prohibitively expensive for now. However, it is not due to the GFET itself anymore, rather the associated measurement tools and parallel structures necessary for recording high-resolution measurements of GFET characteristics. These are measurement tools which currently sell in the USD \$10,000 – \$100,000 range. Graphene is now readily grown by cost-effective Chemical-Vapor-Deposition (CVD) processes in sheets large enough to fully cover any standard Si wafer size. It is readily patterned by lithography and etching processes to make practically any common 2D architecture necessary for Complementary-Metal-Oxide-Semiconductors (CMOS), or addressable gates for Very-Large-Scale-Integration (VLSI) memory to name some of interest.

Ideally, a low-cost means of effective signal sensing and device modulation would help in rapid prototyping. In industry, this is where Field-Programmable-Gate-Arrays (FPGAs) take center stage. Their ease of modification of logical circuits allows for channel integration on microprocessors and other controllers. However, FPGAs are esoteric devices with their own complex programming languages at times. FPGAs are thus usually left for testing on prototypes in their final stages. Testing and screening before attempting larger scale integrations on an inexpensive but effective device has the compounded effect of saving money at every step of development. An inexpensive testing platform would also break down the barriers of access to exposure to advanced electronics for education in the sciences, inspiring a broader pool of the next generation to see themselves as young researchers with a potential contribution to the world.

This report seeks to relay to the reader a simple and inexpensive means of modulation of GFETs with Raspberry Pi (Pi) scientific computing. Using passive and active circuit components to drive a sensor testbed from Millipore Sigma (GRFETS20), the Pi controls the GFET testbed with Python automation and scientific computing. The Pi drives an analog current source control for powering the GFET and a DAC active circuit for gate modulation to control the graphene channel resistance. It measures voltages and stores data and displays graphs of the current sample run for the operator to save from the command line.

This simple prototype testbed is easily modifiable and serves as a proof of concept for mock-ups or more involved devices. Its limitations are, to name a few, its lack of shielded components and parallel conditioning networks necessary for high fidelity signal analysis as well as more involved functionalities that come from Graphical-User-Interface (GUI) control with industry tools. Industry standard measurement tools like Keithley and Keysight have automated triggering and signal capturing as well as internal menus for effective circuit modeling characteristics which would be too involved to prepare for manually controlled rapid prototypes. However, the need for high fidelity measurements and circuit selection control may not be necessary. Especially in sensors for consumer electronics. If the only requirement is to demonstrate control within its expected operational environment and report measures within a tolerable error margin, the most cost-effective circuit capable of such control will always be sufficient.

2. Theoretical Background

2.1 The Quantum Diatomic Molecule

There are several resources which provide formal derivations and discussions on band dispersion relations in general and in graphene as well as background information on the wavefunction theorems discussed later [10]–[12]. A rigorous, deductive approach from these resources is summarized for the reader in this section. Refer to (1) – (4) for an introduction to the quantum models elaborated on in this report.

$$E\psi = i\hbar\frac{\partial\psi}{\partial t} = -\frac{\hbar^2}{2m}\frac{\partial^2\psi}{\partial x^2} + V(x)\psi \tag{1}$$

$$\hat{H} = -\frac{\hbar^2}{2m}\frac{\partial^2}{\partial x^2} + V(x) \tag{2}$$

$$(\hat{H} - E)\psi = 0 \tag{3}$$

$$\psi = \sum c_m\varphi_m \tag{4}$$

From Schrödinger’s wave equation (1) the system of equations for a diatomic molecule AB can be defined. The energy Hamiltonian (2) can be used to simplify (1) to derive (3). The linear combination of atomic orbitals (LCAO) (4) is an important axiomatic condition to validating these theories and will be revisited throughout. By ignoring interelectron repulsion interaction potentials as miniscule and diffuse the classical solution of the free electron model from De Broglie’s relationship being $E = \hbar^2\boldsymbol{k}^2/(2m)$ can be derived by separation of variables of (1). This relation will be compared to the nearly free electron in a periodic potential.

Truncating (4) to a 2nd order approximation of (3) gives the linearized system of equations necessary to solve for the diatomic molecule whose solution can be expressed analytically. The average value of the Hamiltonian, given interaction potentials between the complex wave ψ^* and real wave ψ, in Dirac notation (5) along with (4) and (3) are used to derive (6), the average energy of a diatomic quantum molecular system, where u is substituted for ψ.

$$< \psi^*|\hat{H}|\psi >= \frac{\int \psi^*\hat{H}\psi\, dv}{\int \psi^*\psi\, dv} \tag{5}$$

$$E = \frac{\sum u^*{}_m u_n \hat{H}_{mn}}{\sum u^*{}_m u_n} \tag{6}$$

Solving for each partial differential of (6) with respect to u^* gives (7) and (8), recalling the 2nd order approximation. Setting these derivatives equal to zero gives a set of linear orthogonal equations whose basis can define the eigenvalue energy states. Its orthogonal determinant solution (9) is a quadratic whose roots represent the energy solutions to the diatomic bonding and antibonding states (10).

$$\frac{\partial E}{\partial u^*{}_1} = \frac{\hat{H}_{11}u_1+\hat{H}_{12}u_2-Eu_1}{u^*{}_1u_1+u^*{}_2u_2} \tag{7}$$

$$\frac{\partial E}{\partial u^*{}_2} = \frac{\hat{H}_{21}u_1+\hat{H}_{22}u_2-Eu_2}{u^*{}_1u_1+u^*{}_2u_2} \tag{8}$$

$$\begin{vmatrix} (\hat{H}_{11}-E) & \hat{H}_{12} \\ \hat{H}_{21} & (\hat{H}_{22}-E) \end{vmatrix} = 0 \tag{9}$$

$$E_\sigma = \frac{\hat{H}_{11}+\hat{H}_{22}}{2} \pm \sqrt{\left(\frac{\hat{H}_{11}+\hat{H}_{22}}{2}\right)^2 - (\hat{H}_{21}\hat{H}_{12} + \hat{H}_{11}\hat{H}_{22})} \tag{10}$$

This is, in broad strokes, a solution to one diatomic molecule σ-bonding pair like H_2 and does not serve as a direct description of graphene. This model may be further generalized to include an average polar bonding energy contribution for fractionally ionic and covalent systems however this is not necessary for graphene given its bonding in pure undoped graphene is purely covalent. Refer to **Fig. 1** for an illustration of the band splitting of energy between the bonding σ_g and antibonding σ_u energy levels from (10).

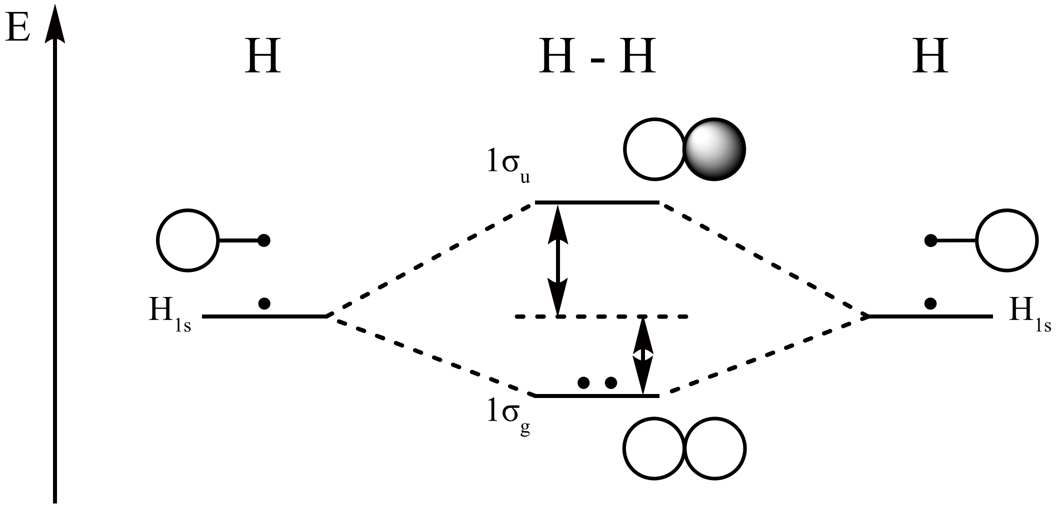

Figure 1. Band energy splitting between bonding and antibonding states from (10). Reproduced with permission from [13].

Consider that a local C-C graphene bond has one filled σ-orbital and one set of hybridized sp^2 orbitals whose solutions as a Schrödinger many-body problem would prove an insurmountable task to express here. Computational models like DFT and Monte-Carlo simulations aid in better understanding the time and space evolution but techniques like this are not necessary for a direct prototyped sensing application and are beyond the scope of this report. Although graphene is not a diatomic molecule, it has symmetrical properties that allow for a local description of a diatomic bond with a more rigorous definition of its location in space. This model does not require any further quantum physics than what has already been discussed.

2.2 Bloch's Theorem, the Brillouin Zone, and Tessellation

To provide a more complete description of graphene as a quantum electronic crystal, symmetry operations must be introduced and performed on the lattice net of graphene to tesselate space. Tessellation is to tile space, covering over 2D space arbitrarily. The mathematics of group theory and its symmetry operations, though useful in defining crystals, will not be discussed here in detail aside from invocations of those operations necessary to define graphene. More important to understanding the concept of the tessellation of space is Bloch's Theorem, named after Swiss physicist and Nobel laureate Felix Bloch, and the concept of a Brillouin-Zone (BZ), named after French physicist Léon Brillouin.

Before discussing these topics any further, it is important to first introduce the concept of reciprocal space. Reciprocal space is, in effect, a region bound by planes defined by vector operations on the vector basis of a given crystal structure. Every crystal structure has a complementary reciprocal lattice, and any crystal structure can be recovered from any reciprocal lattice by applying the same operations on one another. Equations (11) – (13) are used for calculating the reciprocal lattice of a 3D crystal structure. Note that these equations have extra-dimensional variants defined by linear algebra, and that these equations are simplifications thereof. Generalizations to n-dimensional symmetry of these theorems is beyond the scope of this report.

$$\boldsymbol{b}_1 = \frac{\boldsymbol{a_2} \times \boldsymbol{a_3}}{\boldsymbol{a_1} \cdot \boldsymbol{a_2} \times \boldsymbol{a_3}} \tag{11}$$

$$\boldsymbol{b_2} = \frac{\boldsymbol{a_3} \times \boldsymbol{a_1}}{\boldsymbol{a_1} \cdot \boldsymbol{a_2} \times \boldsymbol{a_3}} \tag{12}$$

$$\boldsymbol{b_3} = \frac{\boldsymbol{a_1} \times \boldsymbol{a_2}}{\boldsymbol{a_1} \cdot \boldsymbol{a_2} \times \boldsymbol{a_3}} \tag{13}$$

Moving on, (11) – (13) are used to define BZ, and as such, BZ exists only in reciprocal space. In 2D, BZ geometrically represents the enclosed area of all the perpendicular bisectors of lines drawn between the nearest neighbors in the reciprocal lattice net. In 3D it is the enclosed volume of all the perpendicular bisecting planes of lines drawn between the nearest neighbors. Within BZ, this k-space volume contains all the available wave states for electrons that map to one point and can be shifted upon periodic boundaries. BZ can "unfold" into higher zones to fit more resonant nodes of vibration or more electrons.

Consider that not unrelated to BZ are Wigner-Seitz cells. These cells serve as a visual aid to BZ. They are geometric solids enclosed within a crystalline unit cell which are drawn much the same way as are BZ. Any Wigner-Seitz cell has a corresponding BZ, which is another Wigner-Seitz cell. All 14 Bravais lattices in 3D have a corresponding Wigner-Seitz construction.

So far, the differences between BZ and Wigner-Seitz cells are that BZ exists formally in reciprocal space only, and Wigner-Seitz cells can be formed in both real and reciprocal space. At face value, they are both just a geometric cell in space with a periodic structure. BZ comes into play when defining the Schrödinger system of equations for a lattice net in reciprocal space. Defining these equations within BZ and its boundary conditions tessellates the solution of the system over all space. As such, BZ represent a geometric state distribution in reciprocal space that is directly related to the bonding potentials of atoms in real space. Refer below to **Fig. 2** for an illustration on BZ transformations between face-centered and body-centered crystals in 3D space. Note that they are complementary to each other and are both Wigner-Seitz constructions.

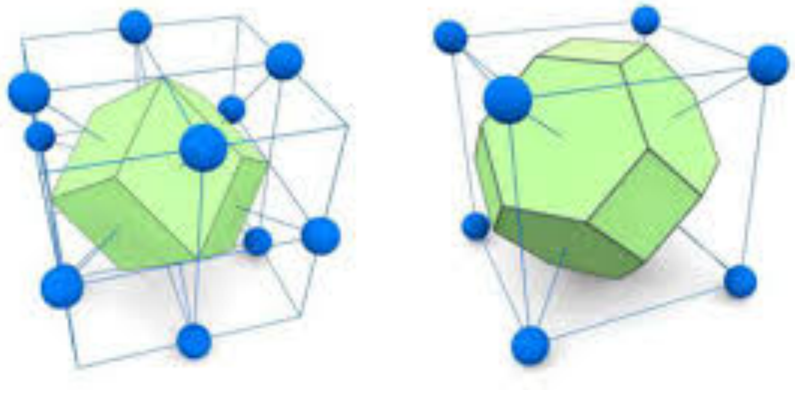

Figure 2. On the left is the FCC Wigner-Seitz cell. On the right is the BCC Wigner-Seitz cell. Reproduced with permission from [14].

Now about Bloch's theorem. Bloch's theorem defines any wavefunction in a quantum crystal as a periodic wavevector. Bloch's theorem is the basis upon which any solution to the Schrödinger equation within a unit cell is periodic, and therefore the solution in BZ is periodic as well. Equation (14) states Bloch's theorem in 1D, where the wave function ψ is defined as a periodic wave function in space that can be shifted by some integer multiple *N* of the periodic lattice parameter a. Using an exponential space wave coefficient here with a periodic term $\boldsymbol{R}$ serves as a periodic wave envelope for ψ.

$$\psi(x + N \cdot a) = \psi(x) = \psi(x)e^{i\boldsymbol{k}\cdot\boldsymbol{R}} \qquad (14)$$

Remember that BZ of a lattice net can be tessellated in reciprocal space. This allows for translation of the local solutions to the dispersion energy band relationships by some integer multiple of the wavevector $\boldsymbol{k} = 2\pi/a$. For any crystalline, periodic structure, Bloch's theorem can be applied to BZ to tesselate the quantum molecular system of equations solutions for all the atoms and their bonds in the lattice net over all $\boldsymbol{k}$-space. The periodic wavefunction ψ from (14) can be transformed into reciprocal space with a Fourier transformation to become (15).

$$\psi(\boldsymbol{k} + \boldsymbol{G}) = \psi(\boldsymbol{k}) = \boldsymbol{C}_{\boldsymbol{k}+\boldsymbol{G}}e^{i(\boldsymbol{k}+\boldsymbol{G})\cdot\boldsymbol{r}} \qquad (15)$$

It is useful to have a prior understanding of Fourier analysis and the convolution of time and the frequency domain. In many similar ways, these same mathematical theorems are applied to convert from space to the reciprocal space BZ. Furthermore, Fourier analysis is at the center of Heisenberg's uncertainty principle and its restrictions on our level of confidence in measurement of an electron's position and its momentum, but this topic digresses the scope of this report and is better suited for a complete course in elementary quantum physics.

More pertinent to the discussion here is the effect of (15), namely the periodic space wave exponential coefficient, on energy dispersion relationships. The exponential $e^{i(\boldsymbol{k}+\boldsymbol{G})\cdot\boldsymbol{r}}$ in (15) bends the bands at periodic multiples of $\boldsymbol{k}$ that would otherwise continue to cross in a parabolic relationship predicted by the free electron model. The bending is related to the applied space wave model of Bloch's theorem. This is what leads to the bandgap of covalent crystals predicted by the nearly free electron model which is observed in semiconductors and insulators. This framework is what will be applied to solving the Schrödinger model for graphene. Refer to **Fig. 3** for an illustration of the effect of band bending and BZ folding in k-space.

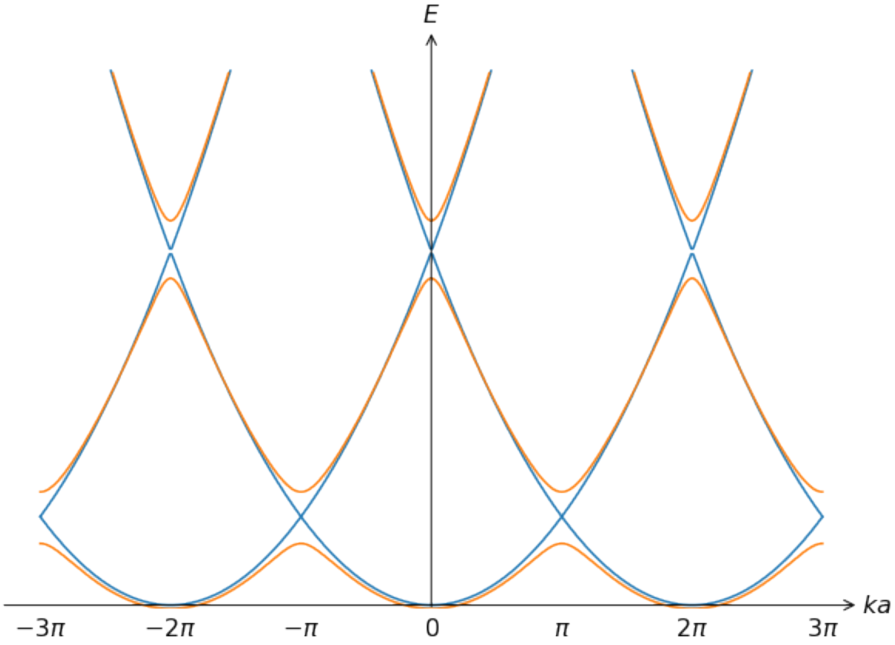

Figure 3. The blue line is the band energy predicted from the free electron model. The red lines follow the nearly free electron model. Reproduced with permission from [15].

2.3 Density of States, Fermi Surface, and Band Bending in Strong Periodic Potentials

Before moving on to applying a framework of physics to graphene it would serve to come full circle and discuss what these dispersion relations mean and how they behave regarding the bulk crystal. From the Pauli Exclusion principle, it follows that no two electrons in a quantum system may have the same energy state or quantum numbers or energy and spin. The Density of States (DOS) is the total number of available energy states for electron occupation for unit volume. It can be derived in ***k***-space by integration over the wave-space domain, and there are several resources for better understanding DOS [10]–[12], [16], [17]. DOS must therefore by Pauli must be a continuum of states as the individual wave orbital energies overlap and cannot be equal. The occupation of the density of states in the valence and conduction bands for covalent crystals are for this reason an important means of classification for different materials, as well as for classifications of defect impurities.

To better understand DOS, it is necessary to understand Fermi-Dirac statistics. This statistical distribution of electron states relates the probability of occupation to the total states available to give DOS. The formal equations will not be discussed here but presented. More importantly, there is an energy level at which the probability of state occupation is at 50% which is predicted from Fermi-Dirac statistics. This energy level is known as the Fermi energy and is crucial to understanding the occupation distribution of energy states in ***k***-space. In a bulk semiconducting covalent crystal, there are DOS for the valence and conduction band respectively. The bandgap energy is the difference in energy between the valence and conduction bands. Refer to (16) – (20) for DOS as well as the Fermi probability distribution and its use for deriving the concentration of majority carriers respectively. Refer to **Fig. 4** for a set of graphs depicting these distributions.

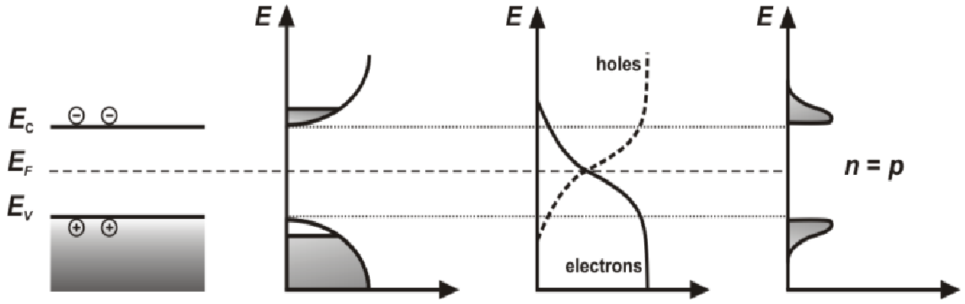

Figure 4. Wavevector bands collapse into the energy domain after integration on the left most. On the left middle the distributions of (16) and (17) are shown. On the right middle (18) and its complementary function are plotted. On the right most is (19) and (20). Reproduced with permission from [18].

$$g(E)_C = \frac{1}{2\pi^2}(\frac{2m}{\hbar^2})^{3/2}(E - E_C)^{1/2} \tag{16}$$

$$g(E)_V = \frac{1}{2\pi^2}(\frac{2m}{\hbar^2})^{3/2}(E_V - E)^{1/2} \tag{17}$$

$$f(E) = \frac{1}{e^{(E-E_F)/(k_B T)}+1} \tag{18}$$

$$n = \int_{E_c}^{\infty} g(E)_C f(E) dE \tag{19}$$

$$p = \int_{0}^{E_V} g(E)_V [1 - f(E)] dE \tag{20}$$

In BZ the Fermi energy is known as the Fermi surface. This manifold is the boundary for 50% probability of occupied and unoccupied states. At absolute zero, on the positive side of the Fermi surface, no states are occupied and on the negative side it is an enclosed boundary domain where all states within are occupied.

It is important to note that the Fermi surface is periodic for a periodic crystal BZ, but it is not necessarily bound by BZ. The Fermi surface may be enclosed by BZ where there are more states available than there are electrons to occupy them. The Fermi surface may also extend beyond BZ in vector directions where there are more electrons filling those states. This is because there is relatively no potential energy barrier for the electrons to populate in that vector direction, or because there is a higher energy penalty for an electron to occupy states in any other direction. This relative change in the potential with respect to vector direction manifests in BZ and is known as band bending in a periodic potential. For a strong potential, the fermi surface may collapse within BZ and behave as an insulator. Refer to **Fig. 5** for a collection of fermi surfaces of select metals in BZ.

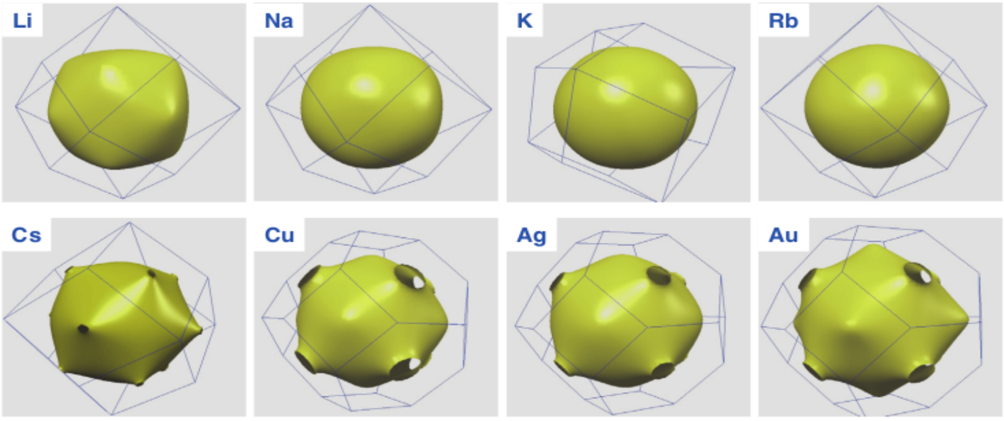

Figure 5. The Fermi surface for alkali metals and some of the precious metals. Reproduced with permission from [19].

When the Fermi surface overlaps in periodic vector directions to the adjacent BZ, this is indicative of transition metal behavior in that vector direction as electrons are not bound to inhabiting states in the local BZ. Materials with Fermi surfaces that do not overlap and are completely bound within BZ may still behave like metals that however conduct through empty states like the alkali metals. The Fermi surface may be bent back within BZ. If BZ is completely full, then the material is a band insulator.

Note in **Fig. 5** that alkali metals with a monovalent electron all have Fermi surfaces enclosed by BZ except for cesium due to the periodic potential becoming weakly bound to its 6s electron. In the precious metals the Fermi surface is overlapping in BZ as is expected for transition metals due to overlapping energy potentials with other bond orbitals. As the atomic number increases the periodic potential begins to deform the Fermi surface for gold to occupy more states than copper and silver. There are far more complex band structures in ***k***-space for d-orbitals in metals than those reported here. It would digress the scope of this report to continue further than this introductory discussion of the physical phenomena at play, however the reader is encouraged to do so.

2.4 Defining a Lattice Net and BZ for Graphene

The International Union of Crystallography (IUCr) publishes updates to their International Tables for Crystallography routinely. Graphene has a 2D planar symmetry net and is *P6mm* group, no. 183 in IUCr [20]. *P* describes first the primitive structural nature, followed by its highest rotational symmetry of *6* about the center of the honeycomb lattice, and 2 mirrors *mm*, orthogonal to both individual basis vectors defined here as ***u*** and ***v***. Refer to **Fig. 6** for an illustration of *P6mm* symmetry group for graphene.

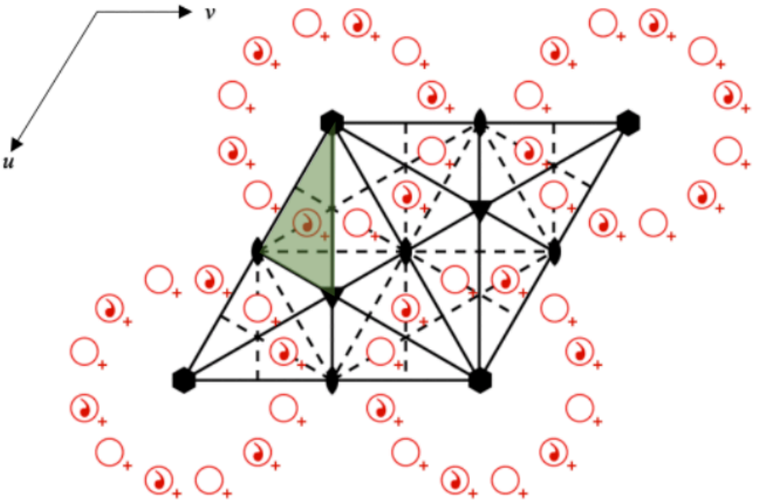

Figure 6. P6mm symmetry group of graphene. The general positions are illustrated as red circles. The area highlighted as green is the asymmetric unit, which can fill the net using the symmetry operations of the group. Reproduced with permission from [21].

Note that the lattice net of graphene is sheared by 30° and its point of origin is at the top-left corner. This shearing transformation may be misleading as it may incorrectly seem that the orthogonal glide mirrors, shown as dashed lines, are not at right angles to the basis vectors, though they are defined to be, and run parallel to ***u*** and ***v*** respectively. The red circles are the equipoints or general positions which show inversion symmetry about the 6-fold rotational points in the net. The 6-fold rotational symmetry points in graphene create 12 identical rotational mirrors by Burger's theorem, and the 3-fold rotational symmetry points are generated automatically by the combination of rotations and translations. 2-fold rotational symmetry points are also generated by mirrors.

In graphene, individual carbon atoms are located at the 3-fold rotational symmetry points $(\frac{2}{3},\frac{1}{3})$ and $(\frac{1}{3},\frac{2}{3})$. The bond length a is the distance between the 3-fold rotational symmetry points. Applying (11) and (12) in graphene converts to $\boldsymbol{k}$-space and defines BZ for graphene with vectors $\boldsymbol{u}^*$ and $\boldsymbol{v}^*$. Refer to (21) and (22) for graphene lattice net basis equations and **Fig. 7** for an illustration of the graphene unit cell and its BZ construction.

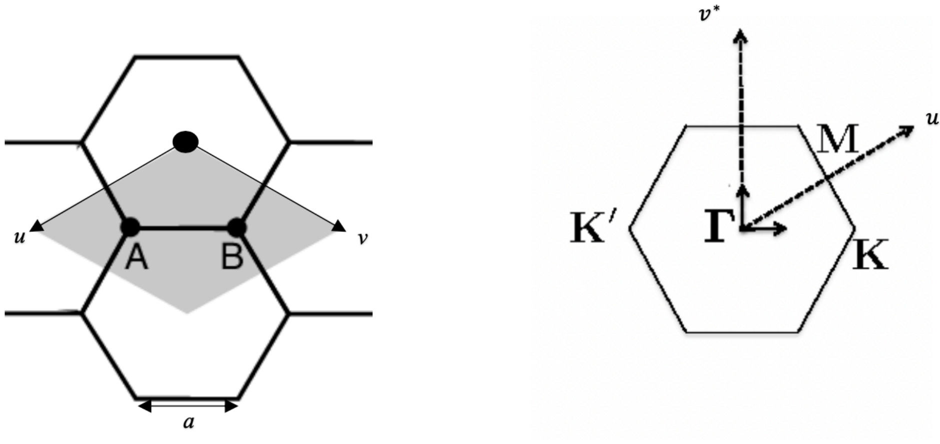

Figure 7. The unit cell and BZ construction of graphene shown respectively on the left and right. Note the bond length and the locations of atoms in the lattice net.

$$<\mathbf{u},\mathbf{v}> = a\sqrt{3} < 1,1 > \tag{21}$$

$$<\boldsymbol{u}^*,\boldsymbol{v}^*> = \frac{1}{a\sqrt{3}} < 1,1 > \tag{22}$$

The points **K** and **K’** in BZ on the right of **Fig. 7** are closely related to the points A and B on the left, where each carbon atom in the lattice net resides in 2D space. **K** and **K’** represent points in $\boldsymbol{k}$-space that are the eigenvector solutions to the energy Hamiltonian that represents graphene BZ in $\boldsymbol{k}$-space. **M** is a metastable energy point in BZ and represents a saddle in the Fermi surface, known as a Van Hove singularity. Electron recombination in **M** requires phonon lattice vibrational activation energies or photon absorption or the activation of semiconducting Moiré superlattices in twisted graphene bilayers. The **Γ** point in BZ represents the nullspace vector where ***k*** is equal to zero.

To solve the energy determinant (9) for graphene the **K** and **K'** points are shifted and set as the local wavefunction and normalized such that $\psi = 1$ at these points. Arbitrary ***k*** wavevectors for ***u*** and ***v*** are chosen to solve for the total sum of the nearest-neighbor bonding pair potentials in the lattice net. Using Euler's theorem, these terms can be canceled and simplified to solve for the band dispersion of graphene. Equations (23) – (26) represent the basis for the Hamiltonian coefficients and the solution to the band dispersion energy from the Hamiltonian determinant adapted from (9). Refer to **Fig. 8** for an illustration of the problem posed for the solutions to graphene BZ within the lattice net highlighted as purple.

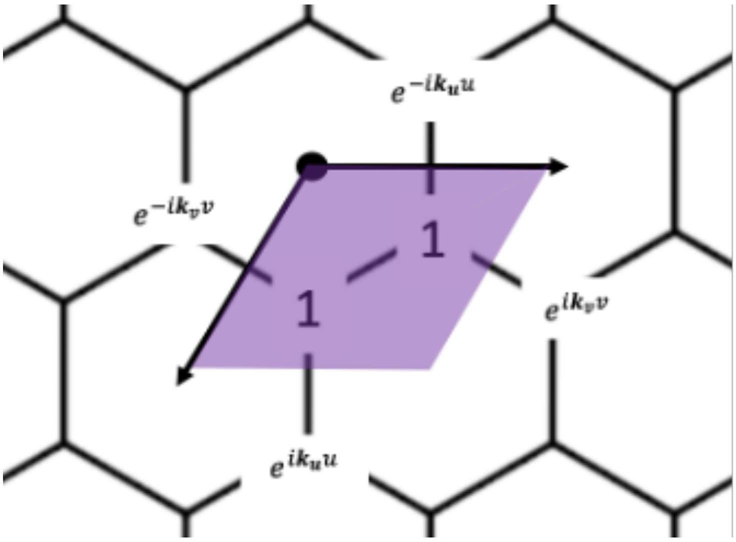

Figure 8. An illustration of the wavefunction terms in BZ for graphene. Effectively, it is an abstraction of the solution to a diatomic homopolar bond from (9) to a more complex system.

$$\widehat{H}_{12} = \beta(1 + e^{ik_u u} + e^{-ik_v v}) \tag{23}$$

$$\widehat{H}_{21} = \beta(1 + e^{-ik_u u} + e^{ik_v v}) \tag{24}$$

$$\begin{vmatrix} 0-E & \hat{H}_{12} \\ \hat{H}_{21} & 0-E \end{vmatrix} = 0 \tag{25}$$

$$E = \pm\beta\sqrt{3 + 2\cos(\boldsymbol{k_u}u) + 2\cos(\boldsymbol{k_v}v) + 2\cos\,(\boldsymbol{k_u}u + \boldsymbol{k_v}v)} \tag{26}$$

The Hamiltonian coefficients for <m|m> intra-atomic bond potentials are set to zero in (25). The Hamiltonian coefficients for <m|n> in (23) and (24) are scaled by an energy potential coefficient β. Equation (26) is the vector sum of bonding potentials in arbitrary wavevector directions. This is the general energy band dispersion of graphene.

Now it is clear from inspection of (26) that when the wavevector $\boldsymbol{k_u} = \boldsymbol{k_v} = 0$, the solution is $E = \pm 3\beta$. This bandgap energy represents the difference in energy between the bonding and antibonding orbitals at the **Γ** point, also known as the zero-point energy.

Setting $\boldsymbol{k_u}$ or $\boldsymbol{k_v}$ equal to zero is setting a complementary solution for (26) in a single arbitrary unit vector direction. If $\boldsymbol{k_u} = 0$ then solving in the $\boldsymbol{k_v}$ direction at the wavevector position $\boldsymbol{k_v} = \pm\frac{\pi}{v}$ for (26) gives $E = \pm\beta$. A complementary solution can be solved for $\boldsymbol{k_u}$ in similar fashion. This is the bandgap energy at the **M** point of graphene, known as the Van Hove singularity.

Furthermore, when $(\boldsymbol{k_u}, \boldsymbol{k_v}) = (\pm\frac{2\pi}{3u}, \pm\frac{\pi}{3v})$ or by exchanging the numerators for $\boldsymbol{k_u}$ and $\boldsymbol{k_v}$ here due to mirroring reflection symmetry, the solution for (26) is $E = 0$. These are the **K** and **K'** points. This implies that at **K** and **K'** the bandgap collapses to zero and graphene behaves like a semimetal, with no energy penalty for conduction. It also implies that the DOS of graphene collapses to zero at **K** and **K'**, with all graphene's electrons occupying a state in covalent bonding. This is what leads to graphene having exceptionally high carrier mobilities and thus high conductivity, but only along the 6-fold rotational symmetry vector directions along the lattice net. Refer to **Fig. 9** for an illustration of the Fermi surface of graphene. Note that the solutions to **M**, **K** and **K'** points are centrosymmetric about the 6-fold rotational point.

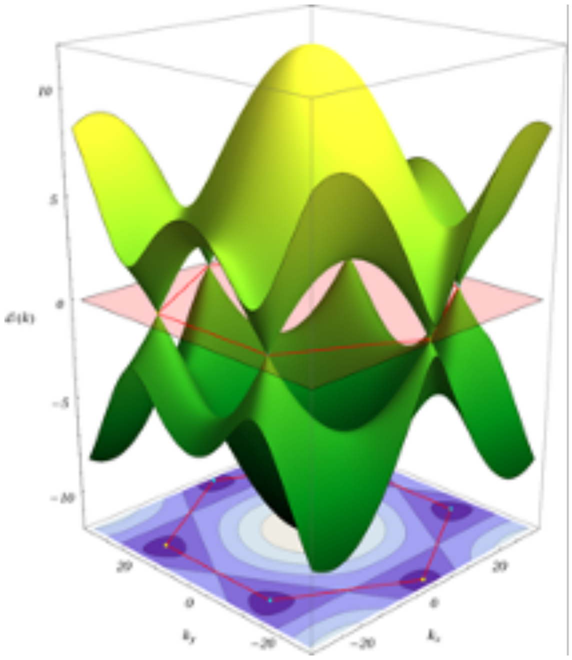

Figure 9. The Fermi surface of graphene. Reproduced with permission from [22].

It's best to pause and relay to the reader now what the implications are for this framework for graphene. Graphene does not conduct like metals do. Where metals in 3D lattices have "gas phase" electrons unbound to the local weak periodic potentials of the ionic cores of their atoms, graphene delivers ballistic electron transport of the delocalized π-bonds along the $\pm u$ and $\pm v$ direction from reflections of the wavefunctions across the lattice net. This is what leads to high conduction in the armchair configuration of carbon nanotubes and graphene as this configuration runs parallel to u and v.

However, the DOS of graphene collapses to zero at the Dirac points, which seems at odds to these predictions of high conductivities. All of this follows from a consequence of the derivation of DOS in 2D (27) which is beyond the scope of this report but is presented for discussion. The classical prediction is still unrealistic and in practice DOS must be adjusted by a Boltzmann thermal energy factor.

$$g(E > E_C) = \frac{m}{\pi\hbar^2}(k_B T) \tag{27}$$

What this implies is that graphene has a distribution of states that are free and available only above the conduction band energy threshold, with all states below occupied and restricted to covalent bonding. Yet, these electrons behave as if there is no energy penalty for their delocalized conduction because there effectively isn't one.

2.5 Doping Effects in Bulk Graphene

Because graphene is a zero-bandgap material and has a single element in its lattice net with theoretically constant electron orbital potentials throughout space, it displays ambipolar conductivity. This means graphene can readily conduct through electrons elevated to the conduction band and by holes generated in the valence band. The adhesion of volatile gas molecules to the graphene surface, ionic electric charge buildup in solution on the graphene surface, and surface chemistry functionalization have all been shown to alter the dopant concentrations in single-layer graphene [4], [9], [23]–[25]. Thus, the adhesion of select target molecules with a characteristic coulombic potential onto graphene has a notable effect on the conductivity and therefore the dopant concentration and the carrier mobilities in graphene. Equations (28) – (30) are on the dopant effects on mobility in graphene, the number of charge carriers at the surface, and conductivity respectively. ${V_G}^*$ is the gate voltage applied at the charge-neutral point of graphene.

$$\mu_{e,h} = \frac{1}{C_{GFET}}\left(\frac{\Delta\sigma_{e,h}}{\Delta V_G}\right) \tag{28}$$

$$n, p = \frac{C_{GFET}}{q}{V_G}^* \tag{29}$$

$$\sigma = q(n\mu_e + p\mu_h) \tag{30}$$

The charge neutral point in graphene is defined to be the minimum conductivity point in graphene with respect to applied gate voltage. It is theoretically the point of ballistic electron transport in graphene where all carriers diffuse in unison however there is much debate and disagreement on the matter [26]. The charge neutral point is readily observable in GFETs with gate modulation used to control the graphene channel conductivity. Refer to **Fig. 10** for a graph of GFET response with gate voltage scan effects from gas molecules.

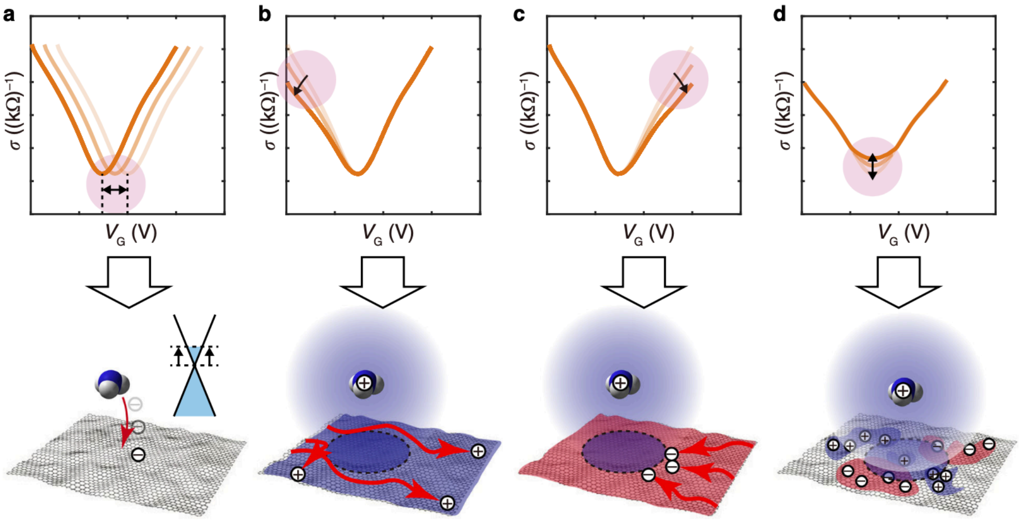

Figure 10. The effects of gas molecule adhesion on conductivity in graphene. Reproduced with permission from [9].

Many previous researchers have noted that the position of graphene's charge neutral point and its magnitude changes with surface adhesion and immersion. Therefore, it follows that the charge neutral point of graphene is more likely related to dopant trap states scattering charge carriers in graphene as it conducts rather than ballistic charge transport.

Refer to **Fig. 11** for the manufacturer's device response characteristics in ambient air for GFET. Note that gas molecules in **Fig. 10** have an effective coulombic potential surrounding the molecule that can displace charges at the surface of graphene. This coulombic potential may have variable polarity depending on its molecule's spatial conformation and may scatter differently for the same molecule depending on the gate voltage. The effect on **Fig. 11** is manifested by varying the circuit response as shown before.

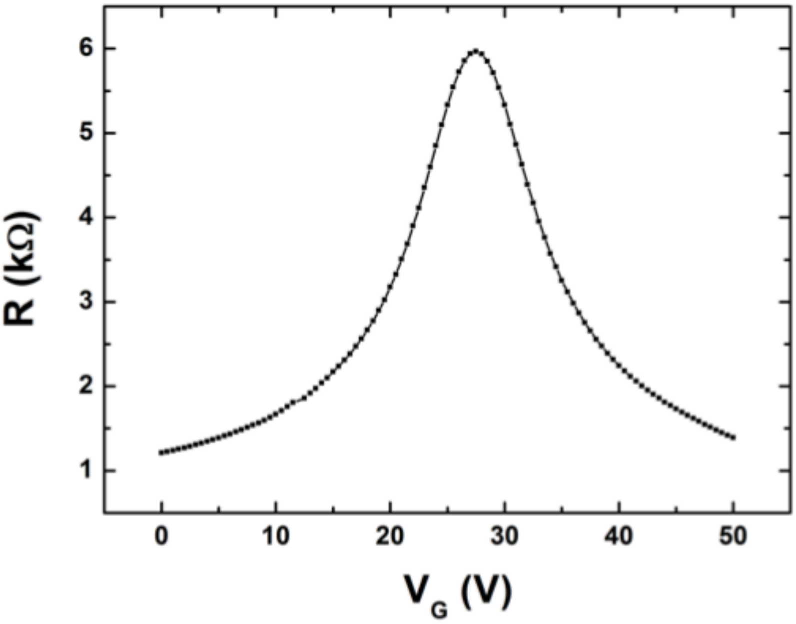

Figure 11. A gate voltage scan across a graphene channel. To the left of the peak there is a dominant hole current and to the right there is a dominant electron current. Reproduced with permission from [27].

Rather than utilizing the charge neutral point gate voltage as a signal it is better to consider the conductivity changes and the associated dopant effects in one regime. The reported gate voltages required are up to 50V and do not lend themselves well to anything other than inert gas environments. Note that the gate voltage need not be so high in liquid immersion setups but does exhibit charge hysteresis after its initial use without cleaning.

Note that the charge neutral point and curvature of the graph in **Fig. 11** are derived experimentally, with no underlying analytical theorem to express conductivity or resistance in GFET devices. From (30), assuming n and p are carrier concentrations per unit area in graphene and for standard mobility from (28), a general prediction of the carrier concentrations in graphene from direct measures of resistance can be made assuming that surface doping of p carriers is stronger at lower operating positive voltages across the gate from **Fig. 10b**. Equation (31) expresses the relationship for reciprocal resistance derived from (28) – (30).

$$\frac{1}{R} \approx qp\mu_h = \frac{\Delta({}^{1}/_{R})}{\Delta V_G} {V_G}^* \tag{31}$$

3. Materials and Methods

3.1 GFET Testbed

The testbed used was a GFET purchased from Sigma-Aldrich (GRFETS20). It is a commonly available architecture that can be sourced from many vendors, though Sigma-Aldrich was chosen to avoid international shipping paperwork from out of USA. It has 12 addressable drain contacts set as 2 rows of 6 (one on the top and bottom), with a common gate and 2 rails for common source. Refer to **Fig. 12** for an illustration of a section of a GFET channel.

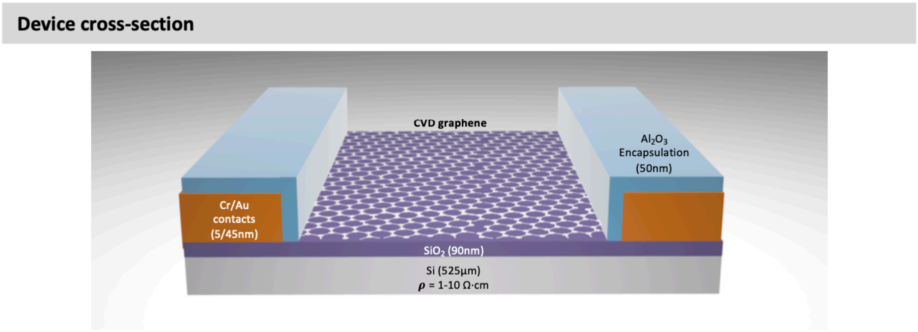

Figure 12. A cross section of a GFET channel not shown to scale. Reproduced with permission from [28].

This surface topology has the added benefit of liquid gating through the top exposed gold electrode. Liquid gating is not necessary for operating the gate as it is bonded to the Si wafer substrate on a chrome-palladium layer over 90 nm SiO_2. This will create a strong charge inversion layer underneath. The surface oxide encapsulation layer of approximately 50 nm of Al_2O_3 comes prepared from the foundry and protects the source-drain leads during liquid gate immersion [28].

The manufacturer suggests that the liquid gate voltage be operated within ±2Vto avoid damaging the gold electrode. however, when operating in inert gas, ambient air, or under relative humidity, voltages of ±5V up to ±15V are not uncommon [27]. Modulation of the gate voltage alters the local electric field beneath the graphene layer and changes the resistance through the channel. Refer to **Fig. 13** for an illustration of the chip.

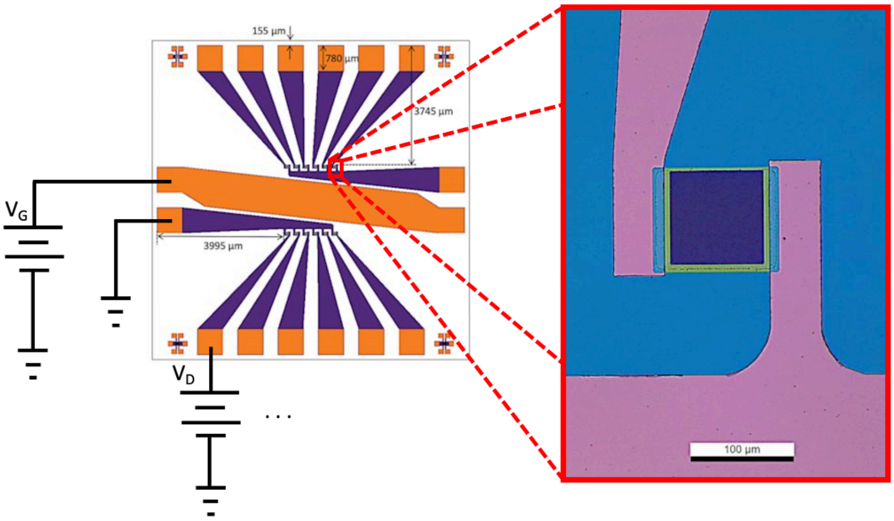

Figure 13. The GFET testbed on the left with a common top gate architecture. The inset on the right is a magnified micrograph of the graphene channel. The device has 12 addressable GFETs with surfaces open to ambient air. The surrounding area is encased in a protective oxide except for the gate and contact pads. Reproduced with permission from [28].

The channel is approximately 100 µm × 100 µm of single-layer graphene with a channel resistance of about 1.2 kΩ [28]. Refer to **Table 1** for a collection of operational parameters and baseline characteristics for GFET.

Table 1. GFET Circuit Characteristics

Sigma-Aldrich GRFETS20	GFET channel parameters
R_{GFET}	~ 1200 Ω[a.]
$\mu_{e,h}$	> 1000 cm^2/Vs[a.]
V_G	±5 V
V_D	~3.0 V
V_S	GND

[a] Value at $V_G = 0$.

It is important to mention now that the Pi is not capable of directly measuring analog voltages as it does not have an on-board ADC like the Arduino controller series does. There are shields available for incorporating this functionality into the Pi for scientific computing [29]. Other projects call for integrating a Pi with an Arduino using ICSP for controlling its ADC directly. However, this setup is slow to communicate and record with the chip registers and does not serve well for the purpose of a high-precision and fast sensor platform. Furthermore, the Arduino has only 10-bit analog read resolution at $\Delta V_{ADC} = 4.883$ mV. This is decent for simple controls but can be improved upon with better components by $\sim 10^6$ for a very competitive cost.

The additional shield for the Pi used here is a commercially available shield for a Raspberry Pi 4 +. The shield works with the ADS1256 24-bit chip for reading analog voltages and converting to digital values [30]. It also comes with an onboard DAC8532 16-bit chip for digital to analog writing control [31]. This high-resolution control allows for fine incremental control and measure of positive monopolar voltages. Its differential mode requires the use of one bit for negative voltage readings, leaving a theoretical read limit at a resolution of measure for reading the ADC at $\Delta V_{ADC} = 596.046$ nV . Writing on the DAC is strictly monopolar with write resolution at $\Delta V_{DAC} = 76.294$ µV. These measures are a theoretical limit to the resolution of control and are the lower limit of expectation. The resolution and error tolerance will be discussed later in full.

The cost is comparable to an Arduino Uno but has various functionalities that complement the Pi and drastically improve upon Arduino. Controlling the ADC/DAC shield is done with a commonly used GitHub library for the Pi using these shields. The chips are monopolar and can only read and write in positive voltages. However, the ADC can operate in differential mode for negative voltage output. The DAC is used to drive a separate monopolar to bipolar circuit to convert to true negative voltages relative to GND.

The drawbacks to this setup come perhaps from it not being able to run as fast as a project running native on an Arduino. Arduino using its C++ libraries can compile its code to run without a head or command terminal and it can do so faster than python for leaner projects. Arduino also has 5 analog read channels. Though the ADS1256 improves upon it with 8 channels, when it is run in differential mode this is split as 4 differential inputs max. However, for this application, the Pi computer's shortcomings in overall achievable speed may not be an issue as controlling GFET requires a simple call and response for reading voltages in separate time intervals.

The benefits gained from utilizing the Pi are a full native Linux based OS running the breadboard with a terminal and HDMI screen and LCD screen which gives a more polished feel to the testbed. Multiple programs can be run from the same testbed as well. With the Pi changing python scripts in the terminal is a better means of changing program runs. It is better than having to upload different sketches to an Arduino that it can only run continuously. Editing scripts was done with Vim and scripts were run directly in the command terminal.

The breadboard circuit controlling GFET uses multiple stages of passive bypass-decoupling with flyback catch to remove the noise of the Pi from signals gathered by the ADC [32]. Capacitive buffering is used directly at the measurement source and at several stages throughout with passive electrolytic and mica capacitors. A twin MAX680 voltage converter power chip setup is used to power an OPA4228 quad op-amp on the breadboard [33], [34]. The MAX680 delivers ± 10V to power the op-amp. The op-amp controls a constant current source powering a full bridge for sensor driving as well as a monopolar to bipolar converter circuit to power V_G with a stepper sine wave or triangle wave control which can be programmed on the python script accordingly. This stepper wave will be monopolar and sweep up to 5V from GND on the Pi. This signal is sent to the op-amp to convert to bipolar $\pm$5V for $V_{G.}$

The current driver for sensing uses a common 2N2222 NPN BJT to deliver a constant current at the emitter terminal [35]. In order to compensate for small amounts of thermal noise and drift an op-amp is connected as a buffering non-inverting follower on the gate of the BJT. The NPN transistor controls a current source with a Zener diode voltage stabilizer. It delivers a small constant current to a Wheatstone bridge for sensing changes to resistance in GFET channels [36], [37]. Resistor values of 1 kΩ were selected to best match the average value of GFET channel resistance. This value was coded into the python script equations for solving the Wheatstone bridge. As the current is split across the full bridge it does not directly matter what the current is, rather how the voltage drops given resistance changes in the bridge. These voltage drops are read and recorded directly by the Pi ADC shield. 2 differential inputs, or 4 single input channels, are required to probe voltages at the Wheatstone bridge. This gives a very accurate measure of the resistance across the graphene channel.

The Pi + shield allows for a total of 2 graphene channels to be addressed by the raspberry pi in one sample run with all 4 differential inputs for high accuracy measures. To collect data here in the earlier development stage, a single graphene channel was addressed by the metal alligator clip and manually moved to a different channel when needed. This is to conserve space on the breadboard and from limitations on the total number of alligator clips that could be attached to GFET without impeding on their neighbors. Once a single measurement run was optimized, the control circuit was modified to multiplex parallel measures of 2 GFET channels. Refer to **Fig. 14 – 15** for full circuit diagrams and component values for the breadboard control circuit.

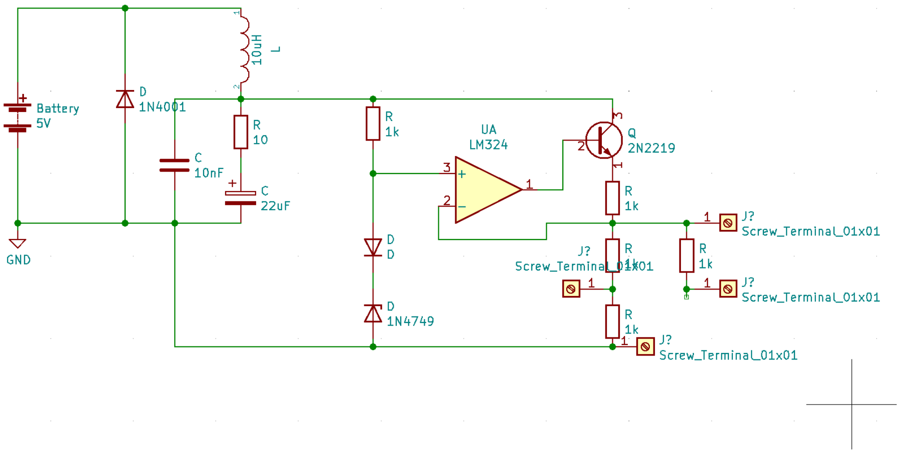

Figure 14. The op-amp control circuit for the current driver that powers GFET.

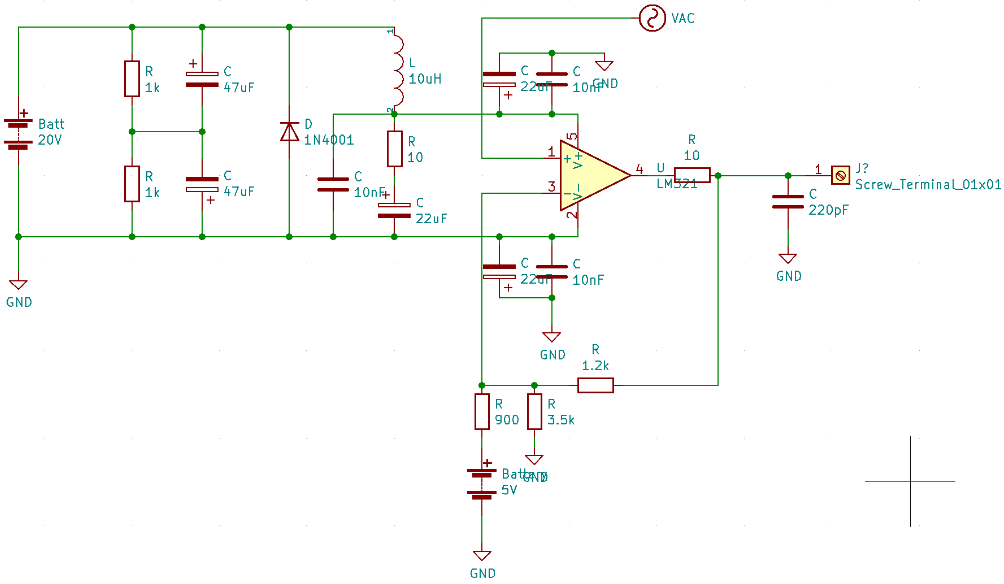

Figure 15. The op-amp control circuit for the gate voltage sweep with the DAC.

3.3 Scan Parameters

The scan program maintains a constant current across GFET and modulates the voltage at the gate as it records events and tabulates results. It was first set as a test sine wave over 100 data points. It takes the Pi less than a minute to complete the scan run, but this depends on the number of tasks the kernel is controlling in the background. Usually running the scan upon booting takes less than 30 seconds to complete. The max voltage for the gate was set as 5V on the scan run. More data points could be added but the pi was found to have a reasonable scan time limit of less than 30 minutes if the total number of collected data points remains fewer than 100,000. A triangle wave with 300 data points was selected for speed testing with overall write resolution at $\Delta V_{DAC} = 20\text{mV}$ steps with a typical scan speed of less than 45 seconds. For sample runs a sine wave was selected for ease of post collection analysis.

In order to control the voltage at the gate, resistors must be manually selected to adjust the scan parameters in **Fig. 14 – 15**. Texas instruments publishes several resources for converting monopolar to bipolar output on their chips [38]. There is a wealth of information online for circuit control with the Pi to rely on as well. The python script used here utilizes many of their guidelines and procedures for connecting sensors for measure.

Equations (32) – (34) used in the python script are the equations for converting the binary signal from the Pi to voltages, along with the written voltage from the DAC, and the conversion to resistance for GFET. The subscripts for V_n are the channels used from the ADC to sense differential measures on the breadboard. These points are the screw terminals in **Fig. 15** where the ADC connects to the breadboard and the alligator clips to GFET.

$$V_{ADC,n} = 5.0\frac{(Channel-n)}{2^{23}} \tag{32}$$

$$V_{DAC} = 5\sin\left(\frac{2\pi}{\mathrm{B}}\vec{x}\right) \tag{33}$$

$$R_{GFET} = R_{1k\Omega}\frac{R_{1k\Omega}(V_1-V_2)-R_{2k\Omega}(V_3-V_4)}{R_{1k\Omega}(V_1-V_2)+R_{2k\Omega}(V_3-V_4)} \tag{34}$$

The addition of the Liquid-Crystal-Diode (LCD) screen with 4-bit mode control as a parameter display uses a popular Adafruit library from GitHub. The LCD was not necessary as the same notifications printed to the LCD are printed to the terminal during the sample run, though it adds to the polished feel of a finished project and makes the scan run process easier to read on multiple places. The display connections could be further simplified with I^2C however the standard 16x2 LCD platform was selected for cost and availability.

The LCD is set up to display directly for the user where the Pi is along during the scan process by printing either "Scan Running" or "Scan Complete" to the bottom row of the screen. A live printout of the resistance value measured can be displayed as well from the tabulated values, but this was left for other projects. Refer to **Fig. 16** for a photograph of the testbed. The inset on the left shows GFET connected by alligator clips to the breadboard.

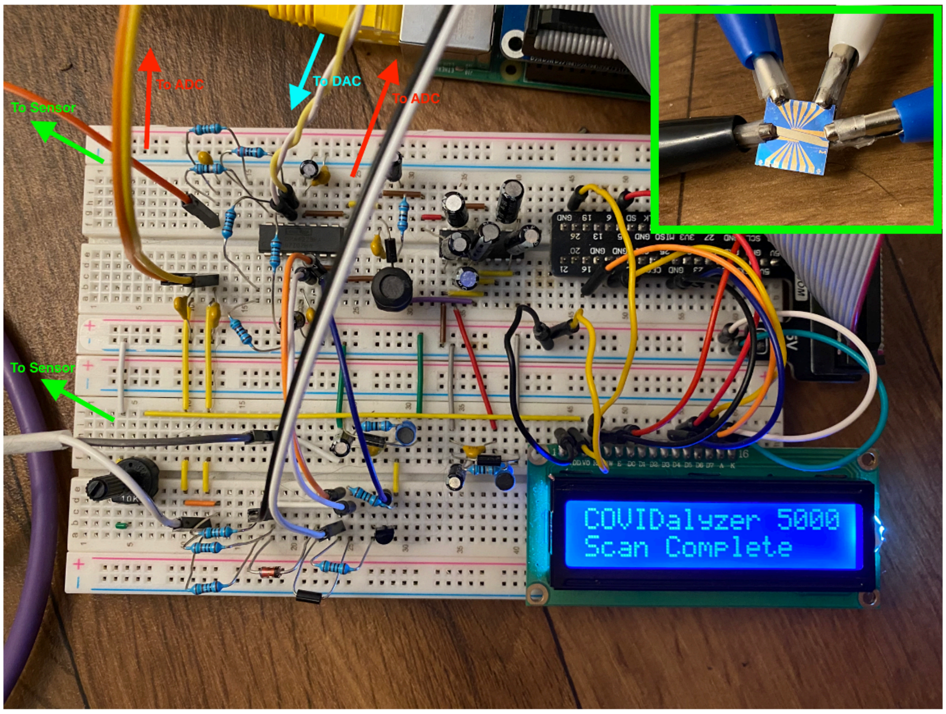

Figure 16. The control circuit built on a breadboard with an LCD display for a mock-up of a portable sensor platform called the COVIDalyzer 5000. Note the inset on the top-left showing the multiplexed GFET connected with clips.

4. Results

4.1 Scan Run Graphical Display Output

Refer to **Fig. 17** for a graph of an early sample run program prepared with the matplotlib module in the python script before sample cleaning.

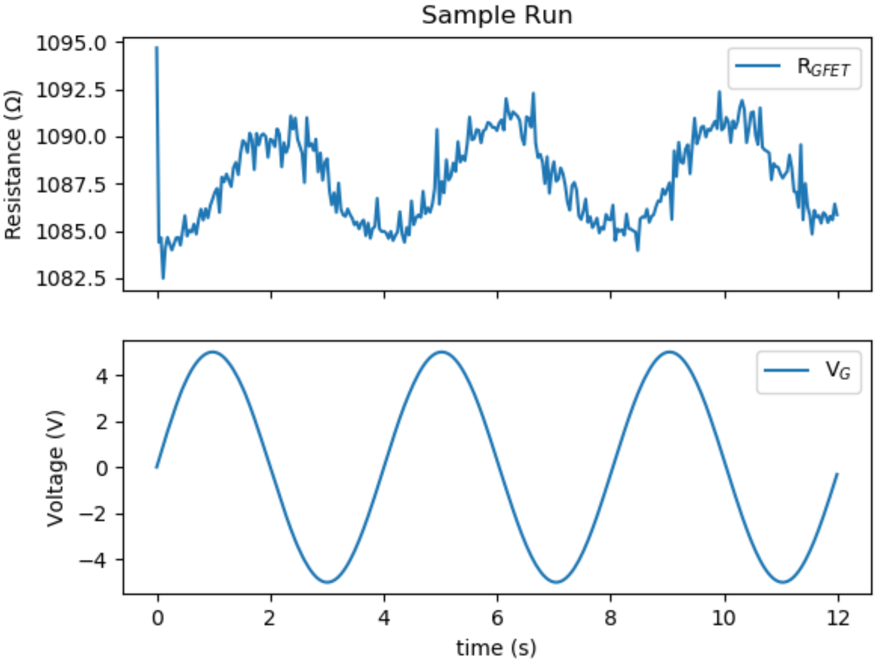

Figure 17. A standardized 3 wave sweep with GFET response on top and the driver signal for the gate voltage below. Note that this scan completes in approximately 12 seconds.

Refer to **Fig. 18** for the final program iteration run on the Pi with a cleaned surface, showing 2 addressed graphene channels and the gate voltage signal.

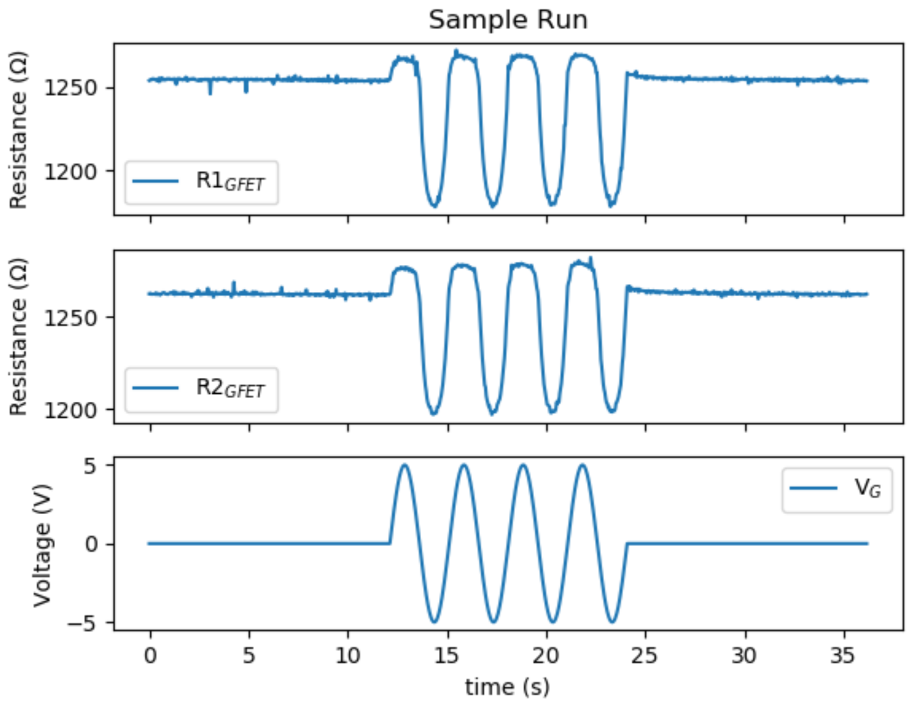

Figure 18. A multiplexed scan of GFET with 2 sensor channels and the gate voltage below. Note that the scan takes about three times as long to complete than before.

4.2 Remote Control with VNC

Refer to **Fig. 19** for screenshots of the Pi desktop controlled remotely with VNC viewer over Local-Area-Network (LAN). VNC was used to run the breadboard remotely and was chosen over SSH for easier graphical display from the Pi terminal. It provides the feel of a finished product with remote access and control available on many common industry tools.

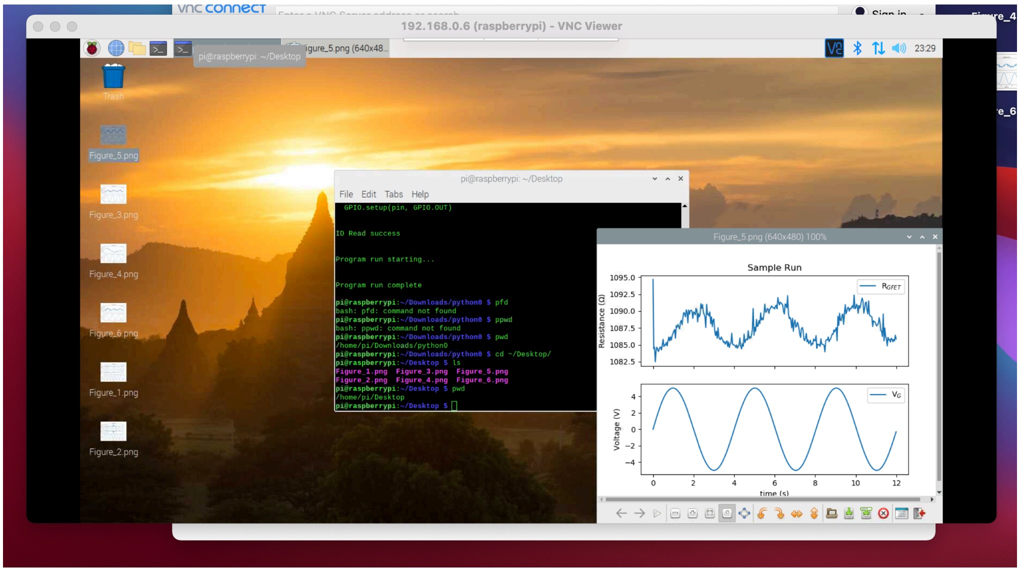

```
  GPIO.setup(pin, GPIO.OUT)


ID Read success


Program run starting...


Program run complete

pi@raspberrypi:~/Downloads/python0 $ pfd
bash: pfd: command not found
pi@raspberrypi:~/Downloads/python0 $ ppwd
bash: ppwd: command not found
pi@raspberrypi:~/Downloads/python0 $ pwd
/home/pi/Downloads/python0
pi@raspberrypi:~/Downloads/python0 $ cd ~/Desktop/
pi@raspberrypi:~/Desktop $ ls
Figure_1.png  Figure_3.png  Figure_5.png
Figure_2.png  Figure_4.png  Figure_6.png
pi@raspberrypi:~/Desktop $ pwd
/home/pi/Desktop
pi@raspberrypi:~/Desktop $ 
```

Figure 19. A screenshot of the Pi after a sample run. Note that the programs are run on terminal and the graphs print directly to the screen GUI.

5. Discussion

5.1 Operational Performance

From **Fig. 17** there was concern of ringing in the circuit. The bypass decoupling stages were found to have a minimal role in the production of a wave envelope and were removed from the breadboard at the GFET powering stages in **Fig.14**. The envelope subsided and the ringing did as well. However, spikes in the signal were found to be outliers and were ignored or selected out from calculations. Further investigation of the noise level led to the decision to revisit data collection after a thorough surface cleaning to remove any leftover photoresist and adsorbed chemicals. The cleaning procedure that was followed was in accordance with the manufacturer suggested procedure from their data sheets.

Fig. 18 shows the data gathered post-cleaning. The signal spikes subsided considerably, and the signal collection became very clear with much less noise. The graph of the scan run shows the final complete procedure, with a baseline calibration phase, signal modulation phase, and a final resting phase. Completing the sample run takes approximately 36 – 45 seconds.

There is clear signal modulation and control of GFET channel resistance by the applied gate voltage. The noise level was studied in the initial and final phases with no gate modulation across GFET in **Fig. 18**. The average value for the sample run channel resistance was found to be on average $R_{GFET} = 1253.958\ \Omega\ \pm\ 0.907\ \Omega$. The background noise of $\pm\ 0.907\ \Omega$ was calculated as one standard deviation from the mean. This was consistent for all the graphene channels.

The level of noise in the prototype is acceptable, given the wide range of channel responses with gate modulation being anywhere from $1000\ \Omega$ to $1300\ \Omega$. The background noise can be ignored or made smooth with interpolation. However, interpolation was decided against during these initial stages so as not to bias the measurements without further study; the data was displayed directly without signal conditioning here.

5.2 Signal Analysis

The sample run of collected data was analyzed in a separate post-collection sample analysis python script. The data gathered during gate modulation was separated and analyzed with various numerical analysis techniques, mainly being the least-squares method applied to a sinusoidal regression. Solving for angular velocity and phase shift was done by way of the golden-search algorithm, which quickly converged to an optimal solution with high precision. The methods used were largely adapted from Moore's and Chapra's texts on numerical analysis with MATLAB, and were adapted *ad-hoc* to compile with python [39], [40]. Refer to (35) – (37) for the linearization basis used to solve for the sine regression used here.

$$f(t_i) = A\sin\big(\omega(t_i - t_0)\big) + D \tag{35}$$

$$\begin{bmatrix} \sum\sin^2(\omega t_i) & \sum\frac{1}{2}\sin(2\omega t_i) \\ \sum\frac{1}{2}\sin(2\omega t_i) & \sum\cos^2(\omega t_i) \end{bmatrix}\begin{bmatrix} A_1 \\ A_2 \end{bmatrix} = \begin{bmatrix} \sum(f(t_i) - \mathrm{D})\sin(\omega t_i) \\ \sum(f(t_i) - \mathrm{D})\cos(\omega t_i) \end{bmatrix} \tag{36}$$

$$t_0 = \frac{\tan^{-1}\left(-\frac{A_2}{A_1}\right)}{\omega} \tag{37}$$

The phase shift t_0 in (37) is the detected variable of interest and is contrasted against the baseline phase of the gate modulation signal. However, further development could lead to sensing by the time evolution of juxtaposed measures in wave attenuation of amplitude *A,* and mean displacement *D*. The mean phase shift was calculated to be $t_0 = -0.055$ s. From (35) this implies that GFET channel resistance leads the gate modulation signal. In brief, suffice it to say that this result agrees with what would be considered a reasonable result; the channel resistance does not respond immediately to gate modulation and the peaks are shifted. Refer to **Fig. 20** for a graph of the analyzed results from one GFET channel.

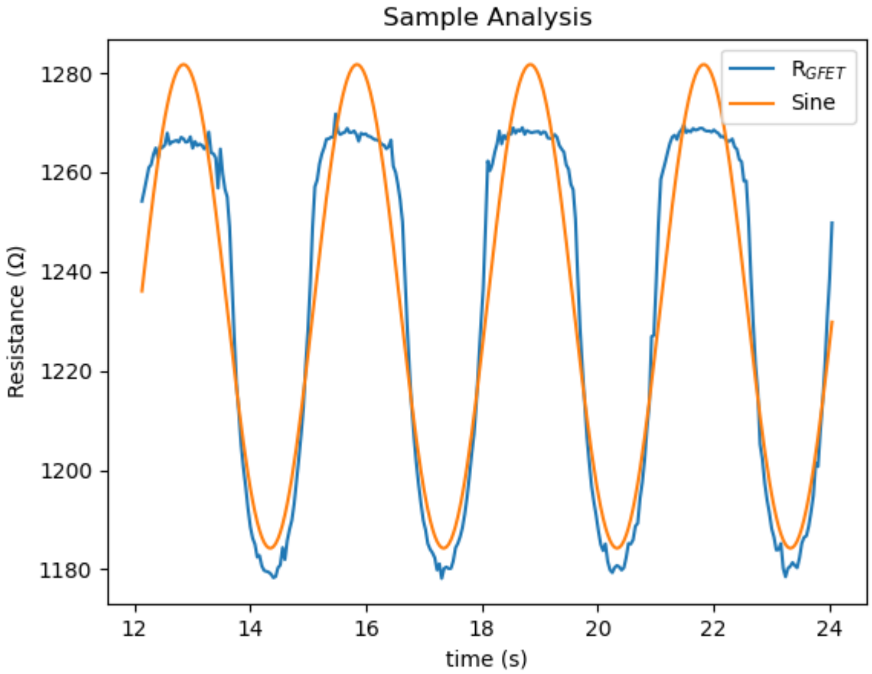

Figure 20. A final display of the scan results from GFET channel with the best-fit wave regression results. The amplitude of the wave is not as important as the phase shift response relative to the input gate voltage signal.

The signal response of GFET to gate modulation displays a clear drop in resistance, or increase in current flow, during negative gate voltage modulation. This behavior indicates the response of GFET is closer to that of a p-channel JFET amplifier. However, GFET response for the expected increase in channel resistance, or decrease in current flow, during positive gate voltage modulation is largely muted. Which is to say, unlike a true p-channel JFET amplifier, a graphene channel alone will not readily close. This is due to the large carrier mobility in graphene readily aiding current flow of generated carriers, and the ambipolar conduction properties of graphene. Therefore, a positive gate voltage bias applied to this device has a marginal effect on driving away holes generated in graphene into depletion and more readily injects electrons into the channel from the source contact.

6. Conclusion

6.1 Summary

It is clear that signal modulation and control of advanced electronics platforms can be done even with simple components for rapid prototypes. GFET control was clear, and the responses were consistent and repeatable. The Pi can collect data, display results even remotely, and can do so with reasonable accuracy for making a sensor platform. The sensors investigated were GFET platforms that responded to control and signal detection within the expected theoretical framework of graphene and are best modeled in their effective response as p-channel JFET devices.

6.2 Future Direction

Moving forward, selectivity and sensitivity for specific chemical targets on graphene should be investigated with this platform. Volatile organic compound (VOC) detection in ambient air or in human breath as trace vapor detection is a popular research and development application for GFETs with proven success in previous research. The compounds are trapped near the surface by various means and alter the electric fields surrounding GFET or play a role in surface doping modulation as well. This would improve upon the signal detections attempted here in **Fig. 20** by adding in discriminatory molecular selectivity for surface vapor adhesion which was a missing complement to the clear sensitivity displayed by the device here.

Acknowledgements

I would like to thank all those researchers who came before me and served as an influence for my studies. In particular I would like to thank Prof. Mehmet Sarikaya of GEMSEC at the University of Washington and Prof. Devin MacKenzie of WCET at the University of Washington for the opportunity to work on this project for them and develop this platform.

I would also like to thank my parents for their love and support, especially my mother for putting me on this path a long time ago when I was much, much younger.

Last, my dog, Zeppelin, who was my only friend throughout the pandemic and global shutdown which restricted our community access to research labs earlier on.

References

[1] Y. Hayamizu, "Bioelectronic interfaces by spontaneously organized peptides on 2D atomic single layer materials," *Sci. Rep.*, p. 9.

[2] D. Khatayevich, T. Page, C. Gresswell, Y. Hayamizu, W. Grady, and M. Sarikaya, "Selective Detection of Target Proteins by Peptide-Enabled Graphene Biosensor," *Small*, vol. 10, no. 8, pp. 1505–1513, Apr. 2014, doi: 10.1002/smll.201302188.

[3] Y. Lu, B. R. Goldsmith, N. J. Kybert, and A. T. C. Johnson, "DNA-decorated graphene chemical sensors," *Appl. Phys. Lett.*, vol. 97, no. 8, p. 083107, Aug. 2010, doi: 10.1063/1.3483128.

[4] D. Kwong Hong Tsang *et al.*, "Chemically Functionalised Graphene FET Biosensor for the Label-free Sensing of Exosomes," *Sci. Rep.*, vol. 9, no. 1, p. 13946, Dec. 2019, doi: 10.1038/s41598-019-50412-9.

[5] M. Sarikaya, C. Tamerler, A. K.-Y. Jen, K. Schulten, and F. Baneyx, "Molecular biomimetics: nanotechnology through biology," *Nat. Mater.*, vol. 2, no. 9, pp. 577–585, Sep. 2003, doi: 10.1038/nmat964.

[6] S. K. Lee *et al.*, "Advantages of a buried-gate structure for graphene field-effect transistor," *Semicond. Sci. Technol.*, vol. 34, no. 5, p. 055010, May 2019, doi: 10.1088/1361-6641/ab0d54.

[7] M. He *et al.*, "Symmetry breaking in twisted double bilayer graphene," *Nat. Phys.*, vol. 17, no. 1, pp. 26–30, Jan. 2021, doi: 10.1038/s41567-020-1030-6.

[8] S. Chen *et al.*, “Electrically tunable correlated and topological states in twisted monolayer–bilayer graphene,” *Nat. Phys.*, vol. 17, no. 3, pp. 374–380, Mar. 2021, doi: 10.1038/s41567-020-01062-6.

[9] T. Hayasaka *et al.*, “An electronic nose using a single graphene FET and machine learning for water, methanol, and ethanol,” *Microsyst. Nanoeng.*, vol. 6, no. 1, p. 50, Dec. 2020, doi: 10.1038/s41378-020-0161-3.

[10] G. S. Rohrer, *Structure and Bonding in Crystalline Materials*, 1st ed. Cambridge University Press, 2004.

[11] D. G. Pettifor, *Bonding and Structure of Molecules and Solids*, 1st ed. Oxford University Press, 1995.

[12] S. Islam and S. S. Z. Ashraf, “Point and Space Groups of Graphene,” *Resonance*, vol. 24, no. 4, pp. 445–457, Apr. 2019.

[13] “Introduction to Quantum Theory.” https://courses.lumenlearning.com/introchem/chapter/the-phase-of-orbitals/

[14] “Crystal Structure,” *Institute of Solid State Physics: Technische Universität Graz*. http://lampx.tugraz.at/~hadley/ss1/lectures18/mar22.pdf

[15] “The nearly free electron model & Bloch theorem,” *Open Solid State Notes*. https://solidstate.quantumtinkerer.tudelft.nl/11_nearly_free_electron_model/

[16] T. Dittrich, *Materials Concepts for Solar Cells*, 1st ed. Imperial College Press, 2015.

[17] S. O. Kasap, *Principles of Electronic Materials and Devices*, 3rd ed. McGraw-Hill, 2006.

[18] “Why is the carrier distribution / density of states different in doped semiconductors.” https://physics.stackexchange.com/questions/497212/why-is-the-carrier-distribution-density-of-states-different-in-doped-semicondu

[19] “Fermi-Surfaces of Alkali-Metals.” https://physics.stackexchange.com/questions/584751/fermi-surfaces-of-alkali-metals

[20] C. P. Brock, *International Tables for Crystallography, 9 Volume Set*, 6th ed., vol. A, 9 vols. Wiley, 2019.

[21] “Space Group 183: P6mm.” http://img.chem.ucl.ac.uk/sgp/large/183az1.htm

[22] “When is the Fermi surface a surface of constant mean curvature.” https://physics.stackexchange.com/questions/77346/when-is-the-fermi-surface-a-surface-of-constant-mean-curvature

[23] S. Lee and Z. Zhong, “Nanoelectronic circuits based on two-dimensional atomic layer crystals,” *Nanoscale*, vol. 6, no. 22, pp. 13283–133, 2014.

[24] P. Lienerth, S. Fall, P. Lévêque, U. Soysal, and T. Heiser, “Improving the selectivity to polar vapors of OFET-based sensors by using the transfer characteristics hysteresis response,” *Sens. Actuators B Chem.*, vol. 225, pp. 90–95, Mar. 2016, doi: 10.1016/j.snb.2015.11.012.

[25] Y.-C. Chang, “Graphene Optoelectronics and Metamaterials,” PhD, University of Michigan, 2016.

[26] S. Adam, E. H. Hwang, V. M. Galitski, and S. Das Sarma, “A self-consistent theory for graphene transport,” *Proc. Natl. Acad. Sci.*, vol. 104, no. 47, pp. 18392–18397, Nov. 2007, doi: 10.1073/pnas.0704772104.

[27] Graphenea, “Graphene Field-Effect Transistor Chip: S20 Measurement Protocols.” Graphenea, 2021.

[28] Graphenea, “Graphene Field-Effect Transistor Chip: S20 Technical Datasheet.” Graphenea, 2021.

[29] Waveshare, “High-Precision AD/DA Board: User Manual.” Waveshare, Oct. 2015.

[30] Texas Instruments, “ADS1256 Datasheet: Very Low Noise, 24-Bit Analog-to-Digital Converter.” Texas Instruments, Semtermber 2013.

[31] Texas Instruments, “DAC8532 Technical Datasheet.” Texas Instruments, Nov. 2014.

[32] Analog Devices, “Decoupling Techniques.” MT-101, Mar. 2009.

[33] Maxim Integrated, “MAX680/MAX681 - +5V to ±10V Voltage Converters,” *Maxim Integr.*, p. 9, Jul. 2019.

[34] Texas Instruments, “OPA4228 HIgh Precision, Low Noise Operational Amplifiers.” Texas Instruments, May 1998.

[35] ON Semiconductor, “P2N2222A - Amplifier Transistors NPN Silicon,” *Semicond.*, p. 9.

[36] B. Carter and L. P. Huelsman, “Handbook of Operational Amplifier Active RC Networks,” *Tex. Instrum.*, p. 85, Oct. 2001.

[37] Texas Instruments, “LM324 Low Power, Quad Op-Amp.” Texas Instruments, Jan. 2015.

[38] K. Duke, “Bipolar +/-10V Analog Output from a Unipolar Voltage Output DAC,” *Tex. Instrum.*, p. 20, 2013.

[39] H. Moore, *MATLAB for Engineers*, 3rd ed. Prentice-Hall, Inc., 2011.

[40] S. Chapra, *Applied Numerical Methods with MATLAB for Engineers and Scientists*, 3rd ed. McGraw-Hill, 2012.